8

Rheo-Particle Image Velocimetry for the Analysis of the Flow of Polymer Melts

José Pérez-González[1], Benjamín M. Marín-Santibáñez[2], Francisco Rodríguez- González[3] and José G. González-Santos[4]

[1]*Laboratorio de Reología, Escuela Superior de Física y Matemáticas, Instituto Politécnico Nacional,*

[2]*Sección de Estudios de Posgrado e Investigación, Escuela Superior de Ingeniería Química e Industrias Extractivas, Instituto Politécnico Nacional,*

[3]*Departamento de Biotecnología, Centro de Desarrollo de Productos Bióticos, Instituto Politécnico Nacional,*

[4]*Departamento de Matemáticas, Escuela Superior de Física y Matemáticas, Instituto Politécnico Nacional,*

México

1. Introduction

The knowledge of the flow kinematics of polymer melts is relevant for basic rheology as well as for polymer processing, particularly for the design of molds and extrusion dies. Nevertheless, the analysis of the flow behavior of polymer melts has been typically performed by using rheometrical (mechanical) measurements and numerical simulation. In spite of the large amount of publications in the field, few works have been dedicated to the analysis of the underlying flow kinematics by using velocimetry techniques. This may in part be due to the difficulties to implement velocimetry techniques during the processing of polymer melts at high temperatures and high pressures.

With the advent of modern technologies that permit the efficient measurement of the velocity of particles seeded in a fluid, it has been possible to obtain velocity maps in fluids, which provide precise details of their flow kinematics. The analysis of flow fields has been mainly done by using optical techniques like laser Doppler velocimetry (LDV), particle tracking velocimetry (PTV) and particle image velocimetry (PIV), which are powerful non-invasive techniques to describe the flow kinematics in transparent fluids. However, while LDV is a single-point measurement technique and PTV requires the tracking of individual particles, PIV is a whole-field method that allows for the determination of instantaneous velocity maps of a flow region. This last approach, of common use in fluid mechanics, has been gradually implemented for the analysis of the flow behavior of polymer melts. Major limitations for the use of PIV in polymer melts rely on the design and adaptation of transparent dies and molds capable to withstand the high temperatures and pressures characteristic of polymer processing operations.

In this contribution, the extrusion of polymer melts is analyzed by using simultaneous rheometrical and two-dimensional particle image velocimetry measurements (2D PIV), or what has been called Rheo-PIV. First, the fundamentals of rheology and rheometry, shear flow and pressure driven flows are introduced. Then, a brief description of flow instabilities and slip in polymer melts is presented, followed by a short account of the work carried out in the study of the kinematics of Poiseuille flows of polymer melts by using optical velocimetry techniques. The geometry and materials of construction of the dies used for velocimetry measurements are highlighted and problems of actual interest in the field, as flow instabilities and slip at solid boundaries, are particularly addressed. Another section includes the basics of the PIV technique, as well as a discussion of some algorithms relevant for calculation of velocity vectors near solid boundaries and high shear gradients regions, which are very common in the flow of polymer melts. Finally, we present some applications of the PIV technique to the study of the stable and unstable Poiseuille flow under slip and no-slip boundary conditions of molten polyolefins with great practical importance, namely, low-density polyethylene (LDPE), polypropylene (PP), high-density polyethylene (HDPE) and linear low-density polyethylene (LLDPE).

2. Rheology

Rheology is the science of deformation and flow of matter. Following this general definition, one might think that rheology is used to analyze any type of material. In practice, however, rheology has been mainly devoted to the study of fluids containing large molecules (macromolecules) or suspended particles, and fluids having a structure, also known as complex fluids. The flow behavior of these fluids cannot be described by the Newton's law of viscosity and are then called non-Newtonian.

Rheometers are based on shear and shear-free flows. Shear-free flows occur when there is not contact of the fluid with solid walls, for instance, during the film blowing or during the elongation of a polymer melt filament. Contrarily, shear flows may be generated by a moving surface into contact with the fluid or by an applied pressure gradient (Fig. 1). For example, that generated in a capillary rheometer.

2.1 The capillary rheometer

Most polymer processing operations and fluid transport take place at high shear rates. In such cases, the rheological characterization of the fluids is performed by using rheometers based on Poiseuille flows, since rotational rheometers are limited to low shear rates. The capillary rheometer is the most used for this purpose; it has a great practical importance since it is found in different polymer processing operations, particularly in extrusion dies and mold runners.

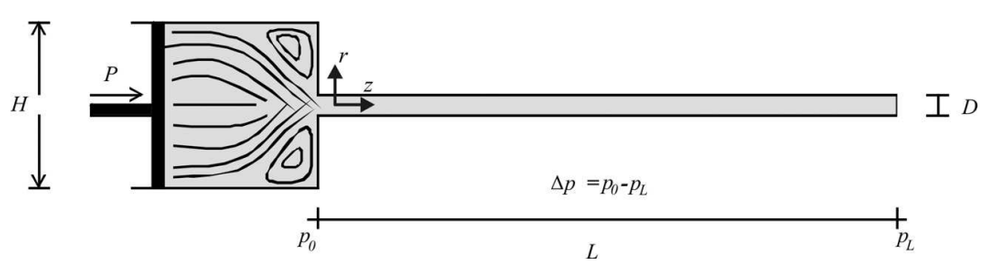

Fig. 1. Schematic representation of a capillary rheometer

The capillary rheometer may be operated at constant pressure or constant flow rate. It consists of a reservoir that holds the fluid to be characterized and a capillary through which the fluid is forced to flow by an imposed pressure (see Fig. 1). The data obtained from this rheometer are the pressure drop (Δp) between capillary ends and the volumetric flow rate (Q). The flow variables, wall shear stress (τ_w) and shear rate ($\dot{\gamma}$), are obtained by solving the momentum and mass conservation equations, respectively, along with a constitutive equation for the fluid (Bird et al., 1977). These equations are solved for isothermal conditions considering the following boundary conditions:

a. Laminar flow
b. Incompressible fluid
c. Steady and well developed flow
d. No-slip at the capillary wall

The assumption of zero velocity at a solid boundary, also known as the no-slip condition, has serious implications from the basic and practical point of view. This condition is generally satisfied for the flow of Newtonian fluids, but is not necessarily valid for some non-Newtonian ones, for example, entangled polymer melts. An investigation of the validity of such condition for the extrusion flow of polymer melts is precisely one of the objectives of this work. Considering the previous assumptions, the shear stress is given by:

$$\tau_{rz}(r) = \tau_w \frac{r}{R} \tag{1}$$

$$\tau_w = \frac{R\Delta p}{2L} \tag{2}$$

where τ_w is the wall shear stress, τ_{rz} is the radial dependent shear stress, r and z are the cylindrical coordinates, R and L are the capillary radius and length, respectively. In practice, the pressure drop (Δp) is not linear between capillary ends due to rearrangements of the velocity profiles at the inlet and outlet region. Then, a correction for end effects is usually applied to the pressure drop (Bagley, 1957). The analysis of such a correction is beyond the scope of this work, but its details may be found elsewhere (de Vargas et al., 1995).

For a Newtonian fluid the constitutive equation $\tau = \mu \frac{\partial v_z}{\partial r}$ is included in the equation of conservation of momentum, which results in a parabolic velocity profile, Eq. 3 (see Fig. 2a), and an expression for the shear rate at the capillary wall given by Eq. 4:

$$v_z(r) = \frac{\Delta p R^2}{4\mu L}\left[1 - \left(\frac{r}{R}\right)^2\right] \tag{3}$$

$$\dot{\gamma}_w = \frac{4Q}{\pi R^3} \tag{4}$$

where Q is the volumetric flow rate given by:

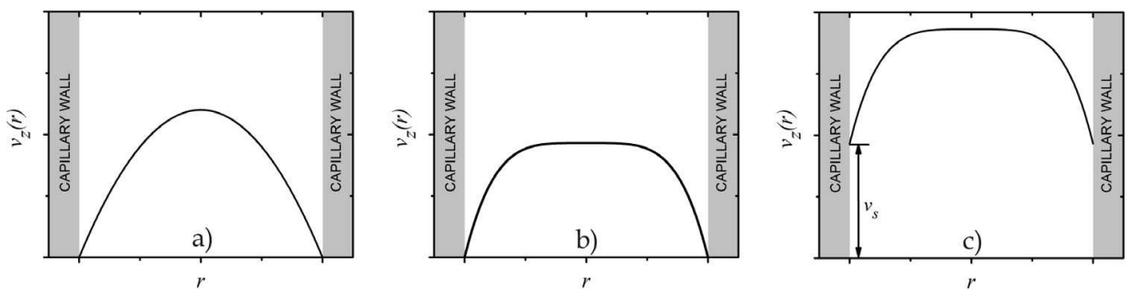

Fig. 2. Velocity profiles: a) Newtonian fluid; b) Non-Newtonian fluid; c) Non-Newtonian fluid with slip at the wall (v_s)

$$Q = 2\pi \int_0^R v_z(r) r dr \tag{5}$$

The fluid viscosity (μ), which is defined as the ratio $\mu = \tau_w / \dot{\gamma}_w$, is given by the well known Hagen-Poiseuille equation:

$$\mu = \frac{\pi \Delta p R^4}{8LQ} \tag{6}$$

For non-Newtonian fluids, the viscosity (η) is dependent on the shear rate, i. e., $\eta = \eta(\dot{\gamma})$ and a commonly used constitutive equation to describe the viscous behavior is the power-law model, $\tau = m\dot{\gamma}^n$, where m and n are the consistency and shear thinning index, respectively. By using this model in solving the motion equations, the fluid velocity (see Fig. 2b) and the corresponding shear rate at the capillary wall are given by:

$$v_z(r) = \frac{nR}{1+n}\left(\frac{R\Delta p}{2mL}\right)^{\frac{1}{n}}\left[1-\left(\frac{r}{R}\right)^{\frac{n+1}{n}}\right] \tag{7}$$

$$\dot{\gamma}_w = \dot{\gamma}_{app}\frac{3n+1}{4n} \tag{8}$$

Where $\dot{\gamma}_{app}$ is given by Eq. 4 and it is referred to as the apparent shear rate when used for non-Newtonian fluids. Eq. 8 is used to calculate the true shear rate and it is obtained after using the Rabinowitsch's correction (Bird et al., 1977).

2.2 Flow instabilities and slip in polymer melts

Flow instabilities restrain rheometrical measurements and limit productivity in polymer processing operations. Unstable flow is obviously unsteady and may produce distortions of extruded materials (see Fig. 3a). Due to these facts, a great deal of work has been devoted to understand and explain the origin of flow instabilities. Most of the research done in the field in the last decades has been thoroughly reviewed by several authors, being some of the most influential reviews those by Petrie and Denn (1976), Denn (1990) and Denn (2001).

Amongst the different flow instabilities, the stick-slip phenomenon occurring in the extrusion of entangled linear polymers melts has received particular attention. This phenomenon starts at a critical shear stress (τ_c) and manifests itself as periodic oscillations of the pressure drop and volumetric flow rate under controlled flow rate experiments. Such oscillations are related to dynamic transitions, from stick to slip, of the boundary condition at a solid wall and produce bamboo-like distortions on the extrudates (Fig. 3a-ii).

The flow curve for a polymer that exhibits the stick-slip instability is discontinuous and is commonly divided into three regions (Fig. 3b). The flow is stable in the first region for $\tau < \tau_c$ (low shear rate branch), unstable for $\tau = \tau_c$ (stick-slip region), and assumed to be stable again for $\tau > \tau_c$ (high shear rate branch). Slip may occur or not in the low shear rate branch depending on the molecular characteristics of the polymer, whereas it is characteristic of the high shear rate branch.

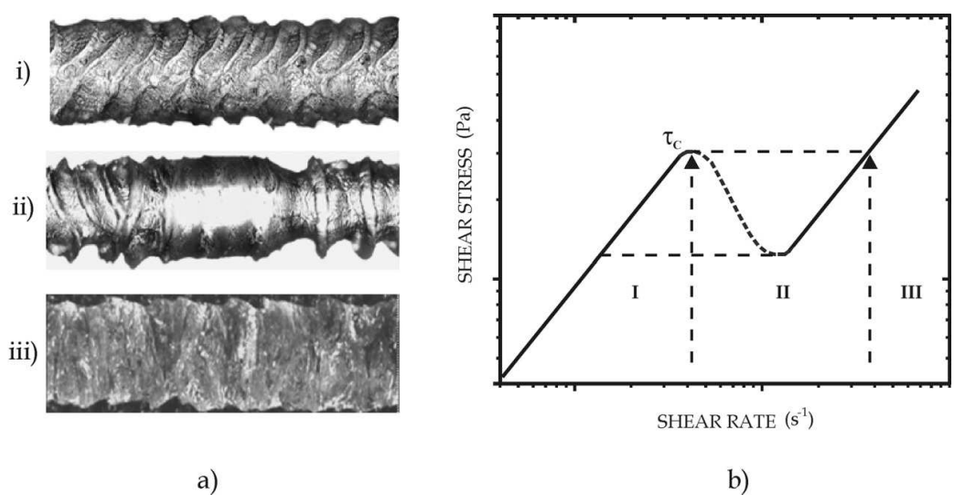

Fig. 3. a) Extrudate distortions: i) Sharkskin, ii) Bamboo, and iii) Gross melt fracture. b) Non-monotonic flow curve.

The assumption of zero relative velocity between a fluid and a solid wall, or "no-slip" condition, has been a matter of debate for a long time. Nowadays, it is widely accepted that such condition may not be satisfied during the flow of entangled polymer melts (see Fig. 2c). The calculation of the slip velocity (v_s), for a given shear stress, has been done by using the Mooney's method (1931), which is a phenomenological correction representing the contribution of slip to the experimentally measured flow rate. According to this, v_s is given by:

$$v_s = \frac{D(\dot{\gamma}_s - \dot{\gamma}_{f-s})}{8}\Big|_{\tau_w} \tag{9}$$

Where $\dot{\gamma}_s$ and $\dot{\gamma}_{f-s}$ represent the shear rates with slip and free of slip, respectively, for a given τ_w. Following this scheme, v_s and $\dot{\gamma}_{f-s}$ are calculated from the slope and ordinate to the origin, respectively, of a linear plot of $\dot{\gamma}_{app}$ versus *1/D* for any given shear stress. The dependence of v_s on the shear stress has been modeled by a linear Navier's condition $v_s = \eta b \tau_w$, where b is a parameter with dimension of length that depends on the fluid-solid

pair into contact (Denn, 2008). Another model for v_s, more often used in numerical simulations with polymer melts, is a power-law, $v_s = k\tau_w{}^p$, where k and p also depend on the fluid-solid pair.

3. Flow kinematics in polymer melts

Despite the large amount of publications about the flow of polymer melts, the experimental description of their kinematics has received scarce attention. Limitations rely on the adaptation of transparent flow geometries capable to withstand high pressures and high temperatures. Following, a short account of the work done on the analysis of the kinematics of polymer melts by using optical techniques is presented.

Early works on the flow kinematics of polymer melts were mainly focused on visualization by using streak photography (Han, 2007), which mainly provides qualitative information on the characteristics of the flow field. In contrast, velocimetry techniques provide not only qualitative, but also quantitative information about the flow field. Accordingly to Mackley and Moore (1986), the pioneer work in the description of the flow kinematics in polymer melts by using velocimetry techniques goes back to the work by Kramer and Meissner, who reported the measurements of velocity profiles for LDPE flowing through and abrupt contraction in a rectangular duct by using LDV. Mackley and Moore (1986) measured the velocity profiles of HDPE during the steady state flow in a slit die with glass windows by using LDV and reported normalized velocity profiles almost insensitive to temperature and flow rate. Piau et al. (1995) carried out LDV measurements in a polybutadiene flowing through a metal slit channel with glass windows and observed slip, characterized by a nearly plug flow, when the die surface was fluorinated. Münstedt and coworkers have made an intensive use of the LDV technique to analyze the flow of polymer melts. Schmidt et al. (1999) analyzed the flow of LDPE through a metal slit channel with a glass wall. These authors obtained the velocity along the channel and measured the length for fully developed flow. Also, they obtained the velocity profiles in the slit and calculated the viscosity from a velocity profile. Later, Wassner et al. (1999) analyzed the secondary entry flow of LDPE in the same channel by using LDV. In a subsequent paper Münstedt et al. (2000) reported what is probably the first detailed description of the velocity profiles during the slit flow of HDPE under stable and unstable conditions by using LDV. Even though their work was limited to a narrow shear rate range, these authors described the typical characteristics of the velocity profiles in the three regimes of the unstable flow curve (see Fig. 3b). A more detailed description of the stick-slip kinematics of HDPE in a slit die, also by using LDV, was provided by Robert et al. (2004). These researchers reported that slip was not homogeneous across the die, then, from a numerical computation, they suggested that the measured slip velocities were of the same order of magnitude as those measured in a capillary rheometer. Combeaud et al. (2007) analyzed the flow of polystyrene under stable and unstable flow conditions at the entry of a slit channel by using LDV. These authors reported periodic oscillation of the velocity corresponding to instabilities and volume distortions in the extruded materials.

In all this set of reports, which are based on single-point measurements, the measurement region (of micrometric size) was generally located by micrometrical displacements in a direction normal to the flow to cover the whole region of interest. This may be very time

consuming and impose limitations for the analysis of fast changing or unsteady flow. On the other hand, slit channels with flat walls have been preferred for measurements, since they do not introduce optical distortions. However, the shear rate in a slit is dependent onto two directions across the channel, so a full description of the flow field requires measurements into two directions, being the slit central plane the proper measurement place to obtain meaningful rheometrical results. In addition, slit channels are typically long and require the use of high pressures to induce flow, which limits the range of shear rates to explore.

Migler et al. (2001) developed a rheo-optics technique to visualize how polymer processing additives (PPA) eliminate sharkskin in a metallocene LLDPE (mLLDPE). These authors measured tracking velocity profiles near the wall and the coating process of PPA in a sapphire capillary, and showed evidence of slip in the coated die and adhesion when this was uncoated. These authors used polydimethysiloxane between the die and an external cube to minimize refractive index variations and to avoid optical distortions. Nigen et al. (2003) studied the entry flow of polybutadiene and its relation with flow instabilities in channel flow by using PIV. Polybutadiene is a low melting point polymer that may be extruded at room temperature, so their analysis does not require special fittings for temperature control. Mitsoulis et al. (2005) analyzed the flow of branched polypropylene in a quartz capillary by visualization combined with laser speckle velocimetry and simulation. These authors showed the formation of vortices in the contraction region and suggested their variation in size with increasing shear rate to be related to the presence of slip in the die. The reported velocity profiles, however, do not exhibit slip. Fournier et al. (2009) characterized the extrusion flow of polycarbonate and polystyrene in a rectangular die with quartz windows by using PIV. The measured velocity profiles in this case, showed good agreement with numerical simulations that considered the influence of slip at the die wall.

The use of capillaries has been generally avoided in studies of the kinematics of polymer melts mainly because of optical distortions introduced by their curvature. However, capillary flow is very often found in rheometry and polymer processing operations. Then, the description of the flow kinematics in such geometry was required. Recently, Rodríguez-González et al. (2009) described for the first time the flow kinematics of HDPE in a glass capillary die by using PIV. These authors corroborated the main results by Münstedt et al. (2000) and Robert et al. (2004) and showed that the velocity profiles cannot become plug-like in the presence of shear thinning in the melt. In a subsequent work (2010) these authors provided clear evidence of alternating behavior between full adhesion and slip in the unstable stick-slip regime of mLLDPE.

4. Fundamentals of PIV

Particle image velocimetry (PIV) has been developed from the early 1980's and can be applied to virtually any kind of flow, as long as the fluid is transparent to enable the imaging the suspended particles. This technique has been developed rapidly over the last three decades and the main findings have been reviewed by Adrian (1991) and Raffel et al. (2007). PIV is a non-intrusive technique commonly used to obtain instantaneous measurements of the velocity vectors in a flow (velocity maps). For two-dimensional PIV, the observation plane is illuminated by a laser light sheet, where two consecutive images of particles seeded in the fluid are obtained. Each image is divided into subsections called interrogation areas, and the statistical displacement of the seeding particles between

corresponding areas of the two images gives the displacement vector. The resulting displacement vector is divided by the time elapsed between the two consecutive images, Δt, to obtain the velocity vector. The seeding particles need to be small enough to follow the flow with minimal drag, but sufficiently large to scatter light to obtain a good particle image. The success of a good analysis is greater when the interrogation areas contain about *8-10* particle images.

Almost all algorithms for estimation of the displacement of a group of tracer particles use cross-correlation techniques. One of the most popular methods is the cross-correlation of two frames of singly exposed recordings. This is a robust method that uses the fast Fourier transform (FFT) to evaluate the cross-correlation coefficient in the interrogation windows. The cross-correlation between the two consecutive images is given by:

$$R(x,y) = \sum_{i=-M}^{M} \sum_{j=-N}^{N} f(i,j) g(i+x, j+y) \tag{10}$$

for $x=0,\pm1,\pm2,\ldots\pm(N-1)$ and $y=0,\pm1,\pm2,\ldots\pm(M-1)$. $f(i,j)$ and $g(i,j)$ are the gray level functions at the position (i,j) of the images taken at time t and $t+\Delta t$, respectively. NxM pixels is the size of the interrogation area. By applying this operation for a range of (x,y) shifts a correlation plane of size $(2N-1)X(2M-1)$ is obtained. The location of the first order intensity peaks in this plane is directly proportional to the mean displacement.

There are two ways to compute Eq. 10; the first is by the evaluation of the cross-correlation function directly by using sum of products. In this case the interrogation windows can have different sizes. Although this approach also reduces the sources of errors, it is rarely used due to the computational cost. The second approach to compute Eq. 10 is via the correlation theorem, which states that the correlation of two functions is equal to the inverse Fourier transform of the complex conjugate product of their Fourier transform. The two dimensional FFT transform is efficiently implemented for an image (2D array of values of the gray scale) using the fast Fourier transform, which reduces the computation from $O(N^2)$ to $O(N^2 log_2 N)$, for a NxN image size. When the FFT is used, it is generally assumed that the data are periodic; this means that the image sample repeats itself in x and y directions. Besides the most common implementation of the FFT needs the interrogation areas are squares of the same size; NxN, with N a power of *2*. There may be two systematic errors in the cross-correlation calculation. One of them is the aliasing; since the input data are considered to be periodic a correlation peak will be folded back in the correlation plane when the data contains a signal exceeding half of the sample size ($N/2$) and appears on the opposite place. Aliasing may be reduced by either increasing the size of the interrogation areas or by decreasing the laser pulse delay. Another consequence of the periodicity of the correlation data is that the correlation estimation is biased; when the shift magnitude increases less data are actually correlated with each other and their contribution to the actual correlation is limited. Computation speed requirements favor in most cases FFT-based correlation, although the aliasing effect and bias error can be present.

The cross-correlation algorithm may produce several peaks and it is necessary to obtain the position and magnitude of the strongest one. Several algorithms to determine the displacement, from the correlation data at subpixel level, have been proposed by Raffel et al. (2007). Three alternatives are the most common; i) the peak position is approximated by the

centroid of the cross-correlation function in the vicinity of the data peak. ii) the digital cross-correlation function, in the vicinity of the peak, is approximated by a known continuous function. The coefficients of the fitting function are found by least squares. The new peak position is taken where the fitting function is a maximum. A parabolic or Gaussian fitting function is used. iii) Finally, the digital auto-correlation around the peak location is computed in a refined grid using an interpolation scheme.

On the other hand, the cross-correlation method only produces an approximation to the velocity field and may be necessary to apply a post-processing to eliminate the wrong vectors (so-called outliers). Detection of either a valid or a spurious displacement depends on the number and spatial distribution of the particle-image pairs inside the interrogation area. In practice, a minimum of four particle-image pairs is required to obtain an unambiguous measurement of the displacement.

4.1 Adaptive second-order accuracy method

Most PIV algorithms use the simple forward difference interrogation (FDI) scheme to calculate the velocity. The velocity at time t is calculated from the particle images recorded at times t and $t+\Delta t$, by using the forward finite difference (Raffel et al., 2007). This approximation is accurate to order Δt and it can be improved by using a central difference interrogation (CDI) scheme, which is accurate to order $(\Delta t)^2$.

Wereley and Meinhart (2001) suggested a PIV technique that performs better than the conventional PIV. The main part of this technique is a central difference approximation of the flow velocity. An adaptive interrogation region-shifting algorithm is used to implement the central difference approximation. Adaptive shifting algorithms also have the advantage of helping to eliminate the velocity bias error. The adaptive central difference interrogation technique has the following advantages over the forward difference approximation with or without adaptation. This technique performs better near flow boundaries or in the presence of velocity gradients because the spatial shift between interrogation areas is based on the local and not on the global velocity. The adaptive method automatically reduces the spatial shift between interrogation areas in regions where the particle displacement is small. In addition, the adaptive CDI technique is more accurate, especially at large time delays between camera exposures and it provides a temporally symmetric view of the flow.

4.2 Data validation

The post-processing of the PIV data is an extensive area and the procedures applied to the vector field depend on the application. At least two stages are necessary for any application; validation and replacement of the incorrect data. When the number of outliers is small their validation can be done by visual inspection and the wrong velocities may be deleted in an interactive way. The spurious vectors are visually recognized by their deviation with respect to the neighbor vectors. Such analysis becomes prohibitive when a great number of recordings have to be evaluated. Then, several automatic procedures have been proposed to validate the raw data. An algorithm that can reject most of the outliers due to noise in the cross-correlation is based on the assumption that for real flow fields the vector difference between the neighboring velocity vectors is small. Typically, a *3x3* neighborhood is used and eight neighbors are used. The vector velocity is rejected if the magnitude of the difference between

the vector and the average over its neighbors is greater than certain threshold. Raffel et al. (2007) used this validation procedure to detect automatically the invalid vectors from the velocity map above an airfoil. Other data validation techniques are found in the literature, however, no general method can be offered for the problem of data validation in PIV. After removing the outliers, it is necessary to replace the missing data. This may be done, for instance, by using bilinear (or bicubic) interpolation from the valid neighbor vectors.

4.3 Velocity bias

Several authors have proposed methods to reduce or to eliminate the velocity bias, which is produced by using equally-sized interrogation areas in the first and the second images. Westerwell (1994) showed that the error bias can be completely eliminated by dividing the image correlation function by the areas correlation function. Keane and Adrian (1992) suggested reduction of the bias by doing the second interrogation area larger than the first, so all particle images in the first interrogation area will likely be contained in the second. They also proposed that spatially-shifting the second interrogation area by an integer part of the displacement will substantially reduce the bias error. Haung et al. (1997) proposed an efficient algorithm to eliminate velocity bias by renormalizing the values of the correlation function in the neighborhood of the peak location prior to calculation of the subpixel peak location. These techniques improve, in general, the PIV results. However, the improvement is limited near to flow boundaries.

To reduce the errors of the displacement estimation, iterative methods have been developed which use a shift of the interrogation areas where the offset can be an integer number of pixels or a fraction (sub-pixel accuracy). If the displacement of the particles of the first interrogation area, between t and $t+\Delta t$, can be estimated, then the interrogation area from the second image can be matched via a relative offset. Scarano and Riethmuller (1999) proposed a method to obtain the displacement and optimize it within an iterative process. Since the components of the predicted displacement, $\Delta s=(\Delta x,\Delta y)$ are an integer number of pixels, their method does not require to use interpolation.

5. Experimental methods

5.1 Materials and rheometry

Molten polyolefins were analyzed in this work, namely, LDPE, PP, HDPE, and mLLDPE, respectively. All the polyethylenes are reported as free of additives that might screen interactions at the die wall and PP is an industrial grade polymer. Their main characteristics are given in Table 1.

Polymer	Melt Index (*g/10min*)	M_w (*g/mol*)	ρ (*g/cm³*)	T_m (°C)	T_{Exp} (°C)	Supplier
LDPE	1.5	---	0.922	115	190	Aldrich
PP	1.8	---	0.9	151	200	Basell
HDPE	0.25	125000	0.950	130	180	Aldrich
mLLDPE	0.8	93200	0.880	60	190	Aldrich

Table 1. Polymer characteristics and experimental conditions

A fluoropolymer polymer processing additive (FPPA, Dynamar™ FX-9613) at a concentration of *0.1 wt.%* was used to produce slip at the interface between the LLDPE melt and the capillary wall. Experiments were carried out at the temperatures given in Table 1 under continuous extrusion with a Brabender single screw extruder of *0.019* m in diameter and length to diameter ratio of *25/1*. The pressure drop (Δp) between capillary ends was measured with a Dynisco™ pressure transducer, whose voltage signal was sent to an independent computer, via an USB data acquisition board, in order to follow the pressure evolution while evaluating the flow kinematics. Pressure data were acquired at a rate of *100* points/s. The volumetric flow rate (Q) was determined by collecting and measuring the ejected mass as a function of time.

Measurements were performed with a capillary die ($D = 0.0017\ m$) made up of borosilicate glass, with an entry angle of 180° and $L/D=20$; no corrections for end effects were performed. This type of glass capillaries has more than *90%* of light transmissibility, high resistance to wear and high dimensional stability under several processing conditions.

A fixture made up of stainless steel was adapted to the extruder die head in order to support a capillary die as shown in Fig. 4a. The fixture has two pairs of perpendicular windows, one pair was used to pass the laser light sheet through the flow region and the other for visualization. Image distortions produced by the curved geometry of the capillary were eliminated by using an aberration corrector, which was made up of a small rectangular prism with glass walls containing a fluid as shown in Fig. 4b. For this purpose, the refractive index (n) of the borosilicate glass capillary ($n_{glass}=1.43$) was closely matched by filling the prism with glycerol ($n_{gly}=1.47$). In order to perform the PIV measurements, one part of the capillary corresponding to a length of *15D* was kept inside the extruder die head at controlled temperature, and the other part of the capillary was inside the aberration corrector, in which the temperature was continuously monitored and supplied with pre-heated glycerol.

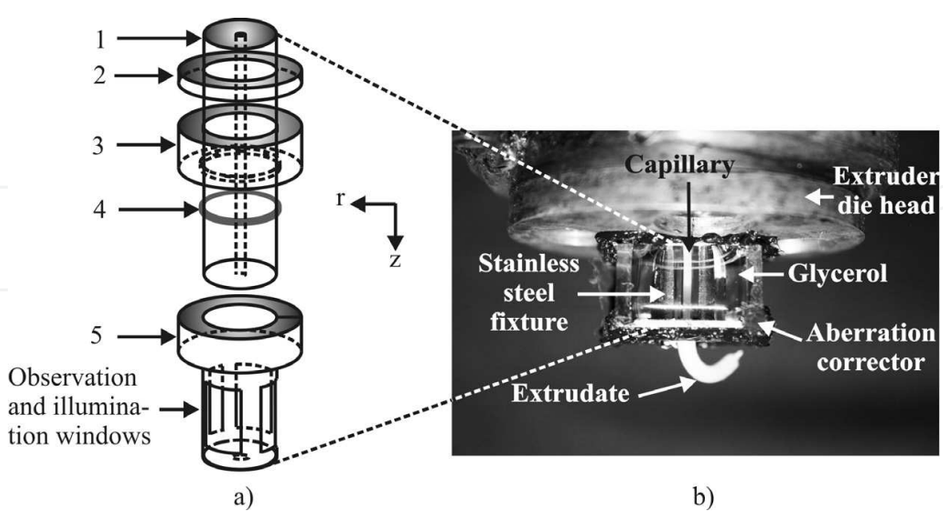

Fig. 4. a) Stainless steel fixture to support glass capillary in the extruder die head: 1) borosilicate glass die, 2) cooper ring, 3) stainless steel ring, 4) high-temperature o-ring, 5) stainless steel fixture. b) Aberration corrector made up of a small rectangular prism with glass wall filled with glycerol.

5.2 PIV measurements

The study of the flow kinematics in the capillary was performed with a two dimensional (2D) PIV Dantec Dynamics system as shown in Fig. 5. The PIV system consists of a high speed and high sensitivity HiSense MKII CCD camera of *1.35 Mega-pixels*, two coupled Nd:YAG lasers of *50 mJ* with $\lambda = 532\ nm$ and the Dantec Dynamic Studio 2.1 software. The light sheet was reduced in thickness up to less than *200 μm* by using a biconvex lens with *0.05 m* of focal distance, and then sent through the center plane of the capillary by using a prism oriented at *45°* relative to the original direction of the laser beam. The prism was mounted on a rail carrier and the center plane of the capillary was found by horizontal displacements of the prism up to see the longest chord on the image plane. The particles used were solid copper spheres < *10 μm* in diameter (Aldrich 32,6453) at a concentration of *0.5 wt.%*. This amount of particles is not expected to affect the rheological behavior of the polymer. Using the Einstein relation for spherical particles in a fluid, the increase in the viscosity due to the presence of copper particles was calculated to be less than *0.1%*, which is negligible.

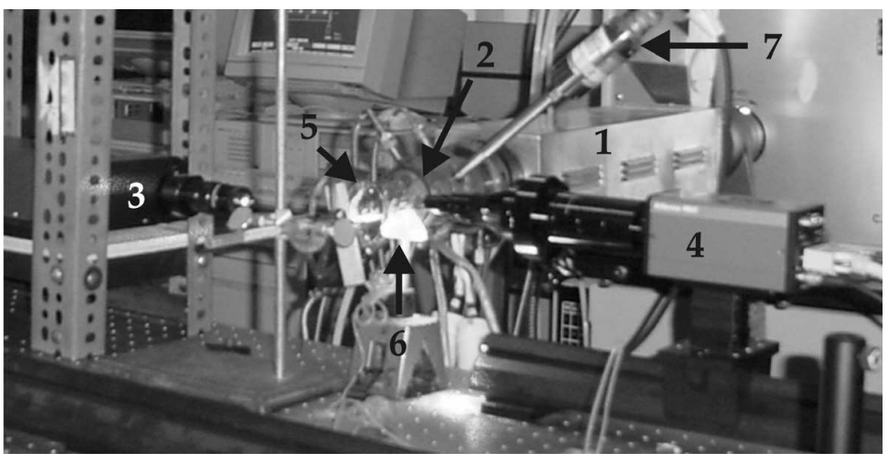

Fig. 5. PIV set up: 1) Single screw extruder, 2) Extruder die head with the stainless steel fixture and the aberration corrector as shown in Fig. 6, 3) Nd:YAG lasers, 4) high-speed and high -sensitivity CCD camera with a continuously-focusable video microscope, 5) biconvex lens, 6) prism, 7) pressure transducer.

An InfiniVar™ continuously-focusable video microscope CFM-2/S was attached to the CCD camera in order to increase the spatial resolution. The depth of field of the microscope at the position of observation was measured as *40 μm*. A small depth of field reduces the true observation volume and the error introduced by out of plane particles. This fact is particularly important in experiments in which the shear stress is not homogeneous, since the wider the light sheet, the bigger the variation of the shear stress in the observation volume. Thus, the variation of the shear stress in the region associated with the depth of field of the microscope was only *5%* of τ_w.

The images taken by the PIV system covered an area of *0.00171 m x 0.0032 m* and were centered at an axial position *z=17D* downstream from the contraction. Series of fifty image pairs were obtained for each flow condition. For stable conditions, the frequency was *6.1 Hz* and all the image pairs were interrogated and ensemble averaged to obtain a single velocity

map. This was not made for unstable regimes where the velocity oscillates with time. In such a case, two frequencies were used, *2.0* and *6.1 Hz*, for slow and fast changes, respectively. The axial velocity component as a function of the radial position (velocity profile) was obtained by averaging the profiles in a map.

According to discussion in subsection 4.1 an adaptive correlation algorithm with a central difference approximation was used to calculate the velocity vectors. This technique has been proved to be more accurate than conventional PIV algorithms when measuring near flow boundaries or in the presence of velocity gradients (Wereley & Meinhart, 2001), which is the case during the evaluation of velocity vectors in the neighborhood of the capillary wall. Since fully developed flow is unidirectional, each interrogation area was chosen as a long rectangle in the flow direction of *256 pixels* long and *16 pixels* wide (*642 μm x 40 μm*, radial and axial direction, respectively), with an overlap of *50%* in both axis. With this width of the interrogation area and the particle size used for seeding, the closest distance to the capillary wall at which measures were made was *40 μm*. Further approach to the wall would require the seeding with smaller particles. Finally, data validation was performed by using a moving average filter.

6. Results and discussion

6.1 Analysis of stable flow conditions

6.1.1 Low-density polyethylene

The rheometrical flow curve for the LDPE is shown in Fig. 6a, along with the one obtained from the integration of the velocity profiles according to Eq. 7. Note that both curves are well fitted by the power-law relationship in the apparent shear rate range studied (see the equation inserted in Fig. 6a). Validation of the PIV measurements is performed via its comparison with rheometrical data. In this case, the data obtained from the velocity profiles agree well with the rheometrical ones; the maximum difference in the volumetric flow rates obtained by using the two methods was *6.5%* at most (the average difference was around *3.4%*), which shows the reliability of the PIV technique to describe the behavior of the polymer melt in capillary flow. The origins of the differences between the two methods are likely found in the location of the laser light sheet with respect to the real central plane of the capillary and its thickness, as well as in the uncertainty of the flow rate measurements.

Figure 6b shows the velocity maps in the capillary for different flow conditions. It is clear that almost all vectors in each map are parallel to the flow direction, which shows that the flow in the observation region was unidirectional for the different apparent shear rates studied, with a velocity field simply given by $v_z=v_z(r)$, as it is expected for a fully developed shear flow.

The PIV velocity profiles for different apparent shear rates are shown in Figs. 7a-b along with the profiles calculated with Eq. 7. Observe that the velocity profiles in the capillary are symmetric with respect to the flow direction and that they are very well matched by Eq. 7. Also, the standard deviation of the time average of fifty profiles, which is represented by the error bars, shows variations below *5%*, which indicates that the flow was steady. It is interesting to note that all the velocity profiles in Figs. 7a-b extrapolate to zero value at the capillary wall, indicating the absence of slip. This result agrees with the well known fact that branched polyethylene melts do not exhibit slip.

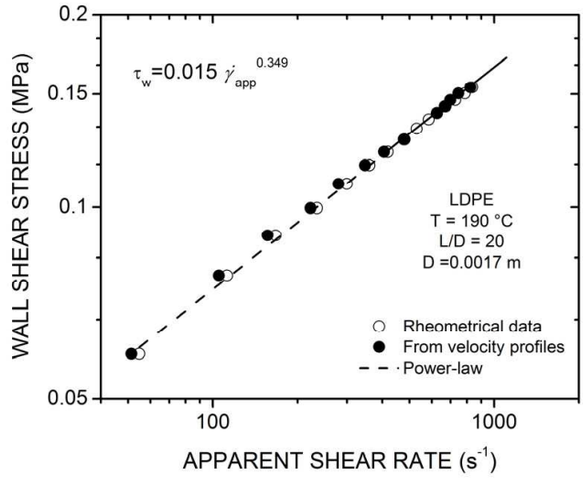

a)

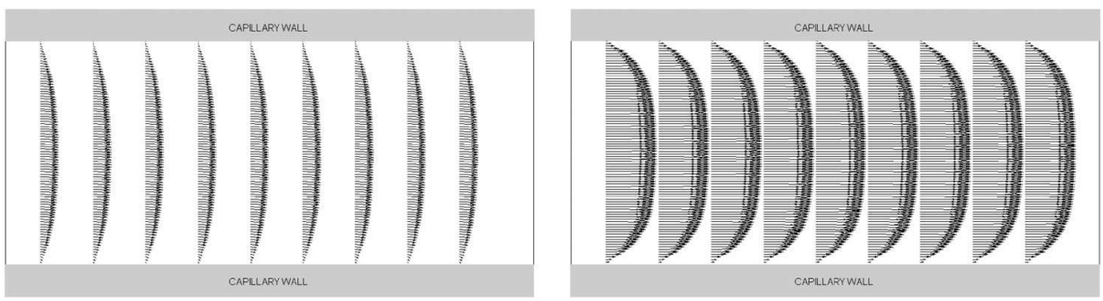

b)

Fig. 6. a) Flow curve for LDPE obtained from rheometrical measurements and by the integration of the velocity profiles. b) Velocity maps in the capillary for different flow conditions.

6.1.1.1 Determination of the flow and viscosity curves from velocity profiles

Due to the radial distribution of the shear stress in capillaries (Eq. 1), i.e., $\tau=\tau(r)$, the true flow curve for a polymer may be obtained from the velocity profiles if a determination of the true shear rate as a function of the radial position is performed. There is a range of shear rates and stresses in a capillary for a given flow rate, namely, $0\leq \dot{\gamma}_r \leq \dot{\gamma}_R$ and $0\leq\tau_r\leq\tau_w$, which enables one to obtain the flow curve from the velocity profiles and the measured wall shear stress. The local shear rate may be calculated from the numerical derivative of the velocity profiles with respect to the radial position. A central difference approximation was used in this work. Meanwhile, the corresponding shear stress was calculated from the measured τ_w by using Eq. 1.

The flow curve calculated by using the velocity profiles corresponding to *54.78, 112.31, 167.1, 359.79* and *834.31* s^{-1}, respectively, is displayed in Fig. 8a along with that obtained by applying the Rabinowitsch's correction to the rheometrical data. The segments of the flow curve reconstructed from the velocity profiles are represented with different symbols for

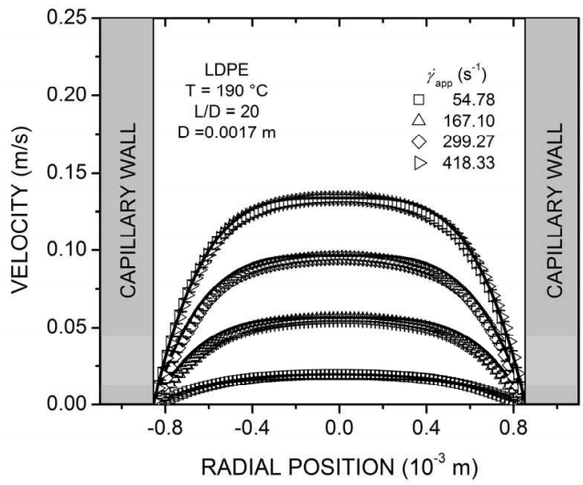

a)

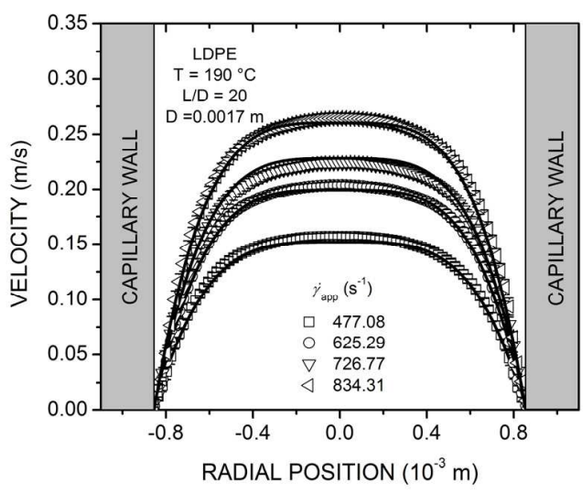

b)

Fig. 7. Velocity profiles for different apparent shear rates for LDPE at a) low and b) high shear rate regimes. Continuous lines represent the power-law model (Eq. 7).

clarity. It is clear that the data obtained from the velocity profiles follow the trend of the rheometrical ones and extend well into the transition between the Newtonian and power-law regions, which is clearly observed in the shear viscosity curve shown in Fig. 8b. The PIV data extend to lower shear rate values than the rheometrical $\dot{\gamma}_w$. This is a valuable fact, since allows the analysis of the low shear rate region that is not accessible by using the macroscopic physical quantities provided by a single capillary. Instead, a rotational rheometer or a capillary of bigger diameter must be used to study the low shear rate behavior.

The wider shear rate range covered by PIV data in Figs. 8a-b permits the fitting of the viscous behavior of the LDPE, $\eta = \eta(\dot{\gamma})$, by a more realistic constitutive equation including the response at low shear rates, as for example the Carreau´s model (Bird et al., 1977).

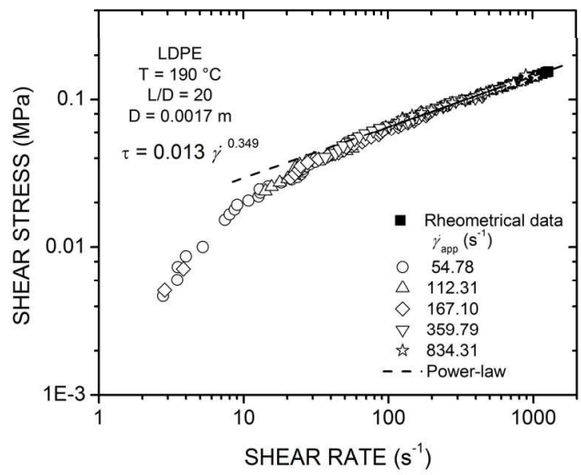

a)

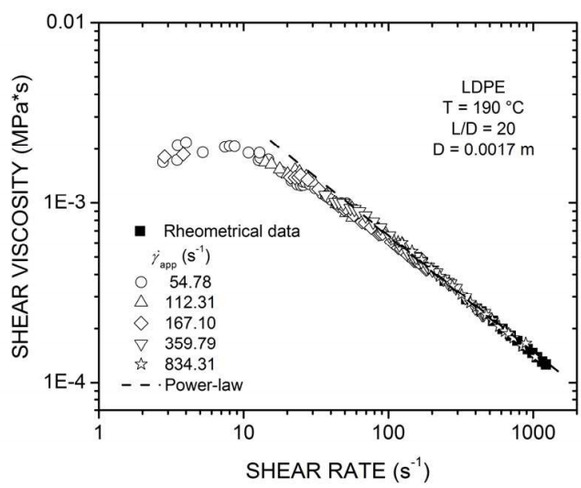

b)

Fig. 8. a) True flow curve and b) viscosity curve for LDPE obtained from local shear rate data. Dashed and continuous lines indicate the power-law and Carreau's model fit, respectively.

6.1.2 Polypropylene

PP shows a similar behavior to the observed for LDPE. The flow curve in Fig. 9a may also be well fitted by a power-law at shear stresses prior to the onset of gross melt fracture, as well as the velocity profiles in Fig 9b. Akin to the LDPE, all the velocity maps (not shown here) agree with a fully developed flow, meanwhile the profiles appear symmetric and extrapolate to zero value at the capillary wall, indicating the absence of slip.

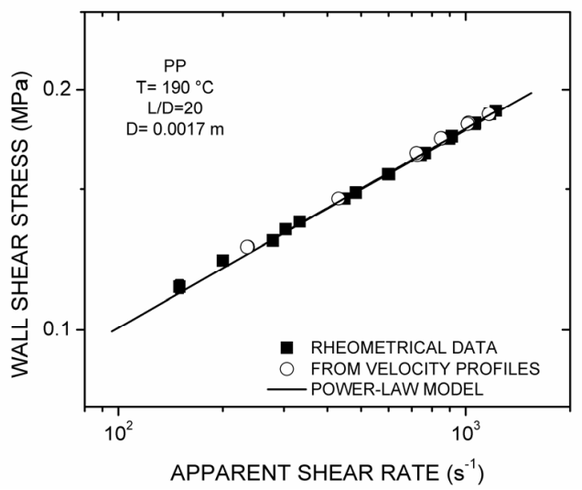

a)

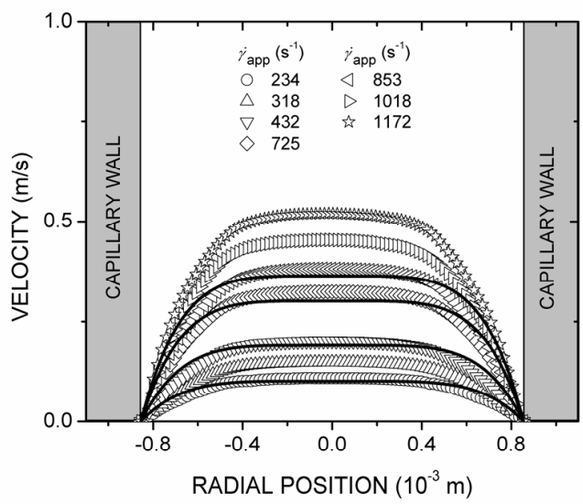

b)

Fig. 9. a) Flow curve for PP obtained from rheometrical measurements and by the integration of the velocity profiles. b) Velocity profiles in the capillary for different flow conditions.

6.2 Analysis of unstable flow conditions

6.2.1 High-density polyethylene

The feature of the PIV technique to produce instantaneous velocity maps, allows for the detection of rapid variations in a region of the flow field. Thus, the PIV technique permits, for example, an accurate description of the flow kinematics under unstable flow conditions occurring in some polymer processing operations. This is particularly the case for HDPE and LLDPE, which are known to exhibit extrusion instabilities like those described in section 2.2 (see Fig. 3a).

The flow curve for HDPE shown in Fig. 10a displays the typical three regions (I-III) of a non-monotonic flow curve (see Fig. 3b). Region I corresponds to a stable flow regime

characterized by a power-law behavior. The stick-slip instability appears in region II; vertical bars represent the amplitude of the pressure oscillations. Region III begins at an apparent shear rate of *652 s*$^{-1}$ and is characterized by the presence of lower amplitude and much faster pressure oscillations than those in region II, which might be related to the onset of the gross melt fracture regime.

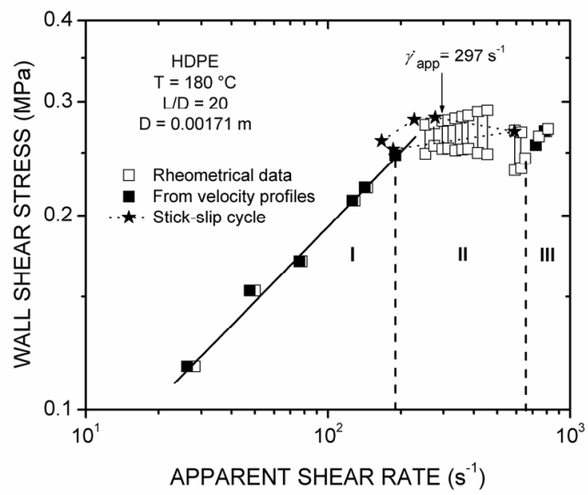

a)

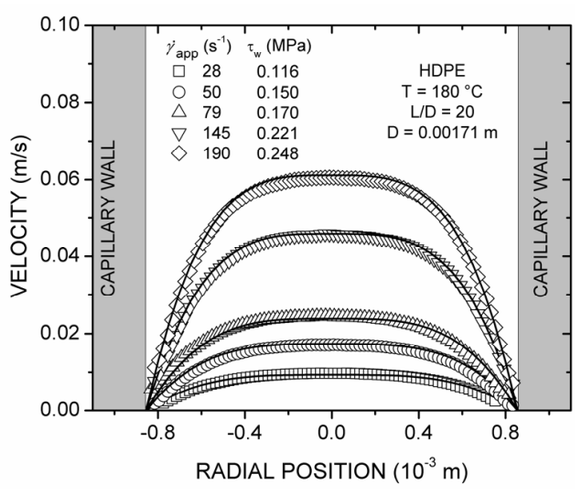

b)

Fig. 10. a) Flow curve for HDPE obtained from rheometrical measurements and by the integration of the velocity profiles. b) Velocity profiles in the capillary for different flow conditions. Reprinted with permission from Rodríguez-González et al., *Chemical Engineering Science*, Vol. 64, No. 22, (November 2009), pp. 4675-4683, ISSN 0003-2509. Copyright Elsevier.

The velocity profiles for the different apparent shear rates in region I are shown in Fig. 10b along with the profiles calculated by using Eq. 7. Also in this case, the flow rate data obtained from the integration of the velocity profiles are included in the flow curve in Fig.

10b. Again, the velocity profiles are very well described by the power-law relationship and there is a good agreement between the rheometrical and PIV data in region I. The velocity profiles in this flow regime do not show slip, even though it is known that HDPE may slip at the die wall. This may be explained by a relatively low molecular weight of the polymer. The magnitude of slip depends on the polymer molecular weight. The higher the molecular weight, the larger the slip velocity.

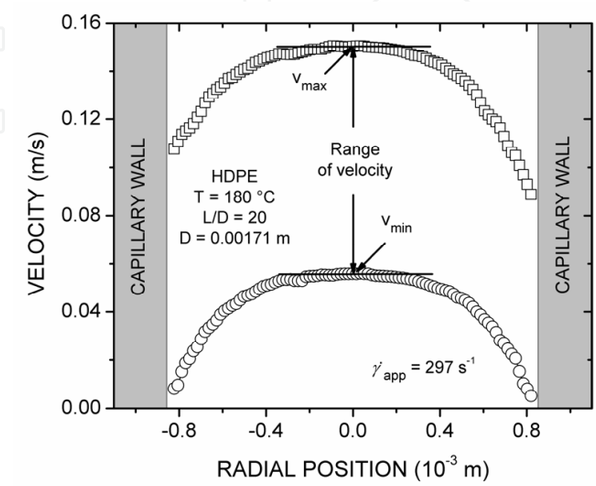

a)

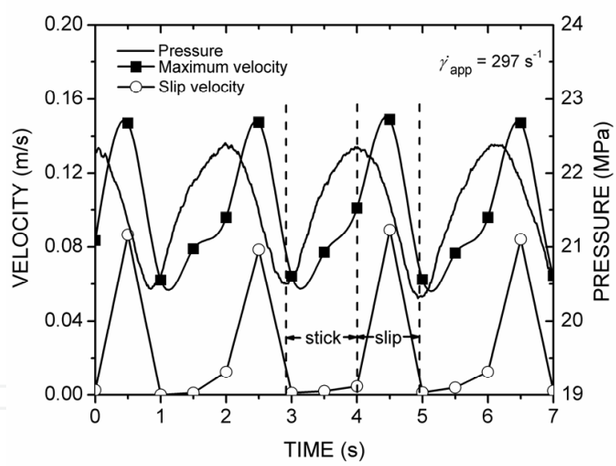

b)

Fig. 11. a) Minimum and maximum velocity profiles during one pressure oscillation at an apparent shear rate of 297 s^{-1}. b) Evolution of pressure, maximum velocity and slip velocity for the same apparent shear rate. Reprinted with permission from Rodríguez-González et al., *Chemical Engineering Science*, Vol. 64, No. 22, (November 2009), pp. 4675-4683, ISSN 0003-2509. Copyright Elsevier.

The pressure signal and the flow maps were recorded simultaneously in the stick-slip regime. The minimum and maximum velocity profiles during one pressure oscillation at an apparent shear rate of *297 s^{-1}* are shown in Fig. 11a. There is a large difference between the maxima of the two profiles, v_{min} and v_{max}, and their values during one oscillation change

from v_{min}=*0.055 m/s* up to v_{max}=*0.151 m/s*. Similar variations in velocity are typical of other apparent shear rates in the stick-slip regime. In addition, the velocity profiles in Fig. 11a show that the boundary conditions change from stick to slip at the capillary wall, in agreement with the term, stick-slip, used to describe this oscillating phenomenon.

Figure 11b shows the evolution of pressure together with the maximum velocity and slip velocity an apparent shear rate of *297* s^{-1}. Note that both, the maximum velocity and the slip velocity, increase continuously during the stick part of the oscillations. In contrast, at the beginning of the slip part of the cycle both velocities rise steeply, reach a maximum and then decrease abruptly up to a minimum at the end of the cycle.

In the high shear rate branch, pressure oscillations decreased in amplitude and became much faster than those in region II. The high frequency of the oscillations in this case did not permit the recording of consecutive velocity maps to describe one full cycle with good resolution (see Rodríguez-González et al, 2009).

6.2.2 Linear low-density polyethylene

The flow curves for the mLLDPE with and without additive are shown in Fig. 12. The flow curve corresponding to the pure polymer resembles that of Fig. 10a; only regions and I-II were explored. Region I corresponds to a stable flow regime that cannot be well fitted by a simple power-law. Instead, a more complex constitutive equation seems to describe the melt behavior. The stick-slip instability appears in region II, the amplitude of pressure oscillations are represented by double points.

Figure 12a also includes the flow curve obtained for the mLLDPE containing additive. In this case, an increase in the flow rate with respect to the pure polymer is evident, as well as the absence of the stick-slip regime. This increase results from interfacial slip between the polymer melt and FPPA. It is noteworthy here that the flow curve for the mLLDPE containing additive also deviates from a power-law and should be fitted by a more complex constitutive equation (Rodríguez-González et al., 2010).

v_s was calculated for the mLLDPE+FPPA system by comparing the data from both flow curves in Fig. 12a using Eq. 9, To use this equation, only stable data from the pure polymer before the stick-slip were considered, assuming them as free of slip. The slip velocity as a function of the shear stress is shown in Fig. 12b. The slip velocity increases with the shear stress and follows a power-law behavior at low shear stresses, but the trend changes as the shear stress is further increased. This change of the rate of increase of the slip velocity along with the shear stress has been attributed to shear thinning of the melt (Pérez-González & de Vargas, 2002).

Figure 13 shows the velocity profiles for the different apparent shear rates in region I. According to the discussion in the previous section, a single power-law relationship was not appropriate to describe all of these profiles. Note that the velocity profiles in this flow regime extrapolate to a zero value at the die wall (no slip), which supports the assumption made in using Eq. 9.

The main results for this mLLDPE agree with those described for HDPE in the previous section. However, an issue to highlight in the analysis of the stick-slip flow of this polymer is the appearance of non-homogeneous slip (Fig. 14a), i.e., the simultaneous appearance of

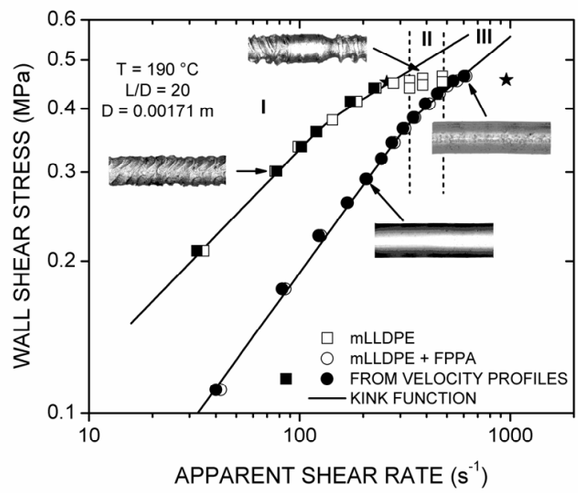

a)

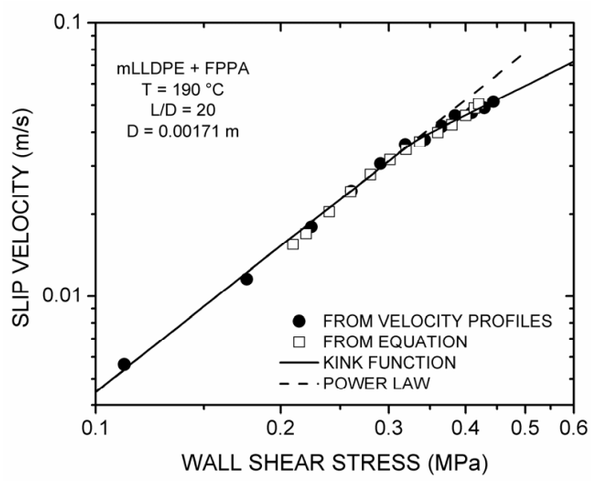

b)

Fig. 12. a) Flow curves for the mLLDPE with and without FPPA. b) Slip velocity as a function of wall shear stress calculated by using Eq. 9 and from velocity profiles. Continuous lines represent kink functions (Shaw, 2007). Reprinted with permission from Rodríguez-González et al. (2010). *Rheologica Acta*, Vol. 49, No. 2, (February 2010), pp. 145-154, ISSN 0035-4511. Copyright Springer-Verlag.

regions with and without slip at the die wall. This new characteristic of the stick-slip flow was recently discovered by Rodríguez-González et al. (2009) in HDPE and it is nicely visualized in the photograph of the extrudate in Fig. 14b. It is noteworthy that these peculiar details of the stick-slip flow may only be detected by instantaneous measurements of the flow field. The detection of this feature of the stick-slip flow is not possible by one point measurements, like in LDV in previous works, but it is allowed by the instantaneous recording of the PIV maps. In fact, the existence of slip during the oscillations can not be assured by LVD, unless a full velocity profile across the plane of interest is constructed.

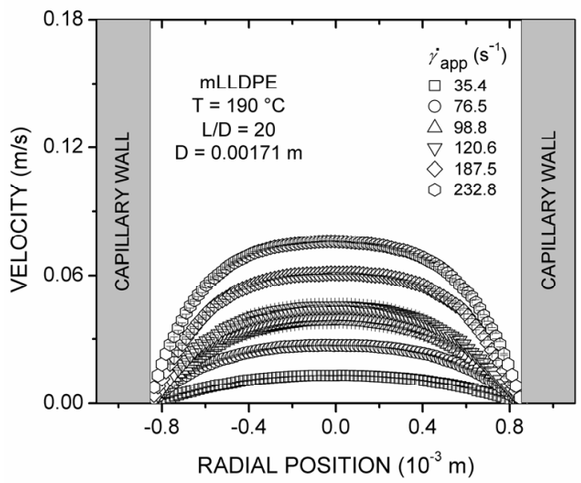

Fig. 13. Velocity profiles for the different apparent shear rates in region I of the mLLDPE flow curve. Reprinted with permission from Rodríguez-González et al. (2010). *Rheologica Acta*, Vol. 49, No. 2, (February 2010), pp. 145-154, ISSN 0035-4511. Copyright Springer-Verlag.

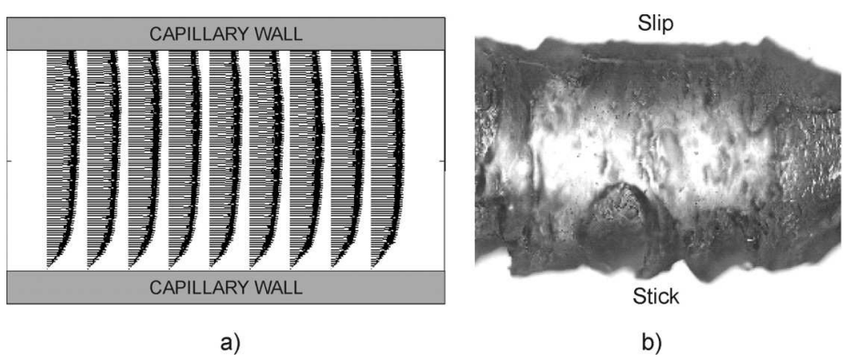

Fig. 14. Non-homogeneous slip characterized by a) velocity map and b) extrudate. Reprinted with permission from Rodríguez-González et al. (2010). *Rheologica Acta*, Vol. 49, No. 2, (February 2010), pp. 145-154, ISSN 0035-4511. Copyright Springer-Verlag.

Figures 15a-b show the velocity profiles obtained for the mLLDPE+FPPA. In contrast to the observed for the pure polymer, the velocity profiles in Figs. 15a-b exhibit a non-zero velocity at the die wall, whose magnitude increases along with the apparent shear rate (shear stress). The slip velocity values obtained from the extrapolation of the velocity profiles at the die wall are plotted in Fig. 12b along with those calculated from the rheometrical data by using Eq. 9. The agreement between both sets of data is remarkable, which provides a direct proof for the validity of Eq. 9.

The relationship between the slip velocity and wall shear stress in Fig. 12b clearly deviates from the power-law behavior at a shear stress above *0.30 MPa*. Then, a more realistic equation, that could be used in numerical calculations, may be obtained by fitting the data to a continuous "kink" function (Shaw, 2007):

$$\log v_s = -1.4276 + 1.7716(\log \tau_w - 5.5202) + 0.0078(1.11 - 1.7716)\ln\left\{1 + \exp\left[\frac{\log \tau_w - 5.5202}{0.0078}\right]\right\} \quad (11)$$

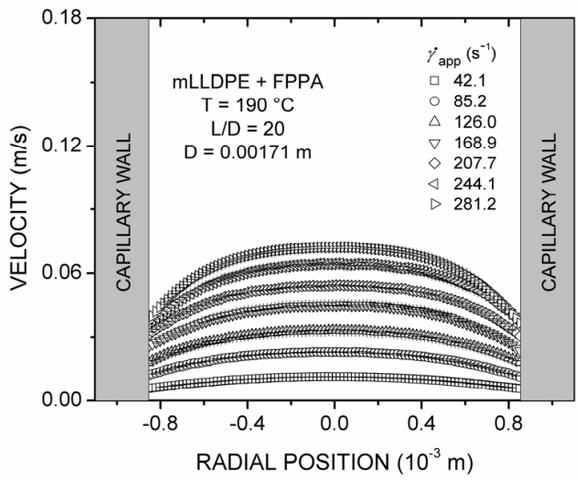

a)

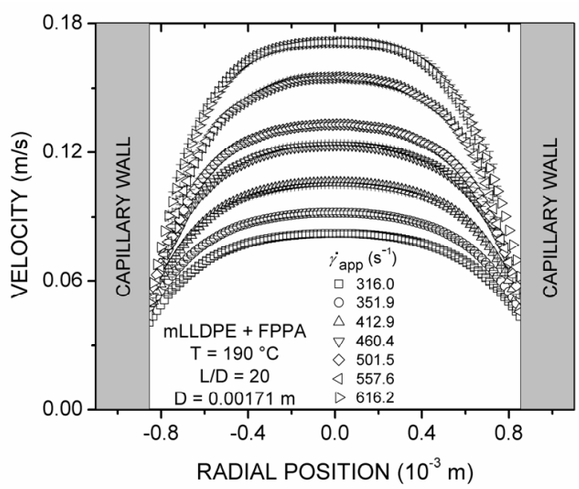

b)

Fig. 15. Velocity profiles obtained for the mLLDPE under strong slip conditions at a) low and b) high shear rates. Reprinted with permission from Rodríguez-González et al. (2010). *Rheologica Acta*, Vol. 49, No. 2, (February 2010), pp. 145-154, ISSN 0035-4511. Copyright Springer-Verlag.

A comparison of the slip velocity calculated by using the kink function (Eq. 11) and a power-law (see Fig. 12b) at τ_w= *0.443 MPa* leads to an overestimation of *23%* in v_s when using the power-law model. Considering the trend in Fig. 12b for the slip velocity, the error introduced by using a power-law model for this polymer will become even more significant at higher shear stresses.

7. Conclusion

The extrusion of polyolefins of significant practical importance, namely, LDPE, HDPE, PP and LLDPE, was analyzed in this work by using simultaneous rheometrical and two-dimensional particle image velocimetry measurements (2D PIV), or what has been called

Rheo-PIV. The results in this work show that PIV is a reliable tool to describe the flow kinematics of this sort of fluids under stable and unstable flow conditions, including the flow with slip at the die wall. Moreover, the use of the PIV technique enables the detection of characteristics of the flow that are not distinguished by using other optical velocimetry techniques like PTV or LDV. The main limitation in the use of PIV for the analysis of polymer processing operation is the need to adapt transparent molds and dies able to withstand high temperatures and pressures. In spite of this, in general, the use of the PIV has a promising future in the study of polymer melts and other complex fluids.

8. Acknowledgment

This work was supported by SIP-IPN (20111119). J. P.-G. and J. G. G.-S. are COFFA-EDI fellows. B. M. M.-S. had a fellowship under the CONACyT's program for the *Apoyos Complementarios para la Consolidación Institucional de Grupos de Investigación* (Sol. 147970).

9. References

Adrian, R. J. (1991). Particle-imaging techniques for experimental fluid mechanics, *Annual Review of Fluid Mechanics*, Vol. 23, (January 1991), pp. 261-304, ISSN 0066-4189.

Bagley, E. B. (1957). End corrections in the capillary flow of polyethylene, *Journal of Applied Physics*, Vol. 28, No. 5, (May 1957), pp. 624-628, ISSN 0021-8979.

Bird, R. B.; Armstrong, R. C. & Hassager, O. (1977). *Dynamics of polymeric liquids, Fluid Mechanics*, Vol. 1, John Wiley & Sons, ISBN 0-471-07375-X, United Sates of America.

Combeaud, C.; Vergnes, B.; Merten, A. & Hertel, D. (2007). Volume defects during extrusion of polystyrene investigated by flow induced birefringence and laser-Doppler velocimetry, *Journal of Non-Newtonian Fluid Mechanics*, Vol. 145, No. 2-3, (September 2007), pp. 69-77, ISSN 0377-0257.

Denn, M. M. (1990). Issues in Viscoelastic Fluid Mechanics, *Annual Review of Fluid Mechanics*, Vol. 22, (January 1990), pp. 13-32, ISSN: 0066-4189.

Denn, M. M. (2001). Extrusion instabilities and wall slip, *Annual Review of Fluid Mechanics,* Vol. 33, (January 2001), pp. 265-287, ISSN 0066-4189.

Denn, M. M. (2008). *Polymer melt processing*. (1st Edition). Cambridge University Press, ISBN 978-0-521-089969-7, United States of America.

de Vargas, L.; Pérez-González, J. & Romero-Barenque, J. (1995). Evaluation of end effects in capillary rheometers for solutions of flexible polymers, *Journal of Rheology,* Vol. 39, No. 1, (January 1995), pp. 125-137, ISSN 0148-6055.

Fournier, J. E.; Lacrampe, M. F. & Krawczak, P. (2009). Characterization of extrusion flow using particle image velocimetry, *eXPRESS Polymer Letters,* Vol. 3, No. 9, (September 2009), pp. 569-578, ISSN 1788-618X.

Han, C. D. (2007). *Rheology and processing of polymeric materials.* Vol. II. (1st Edition). Oxford University Press, ISBN 978-0-19-518783-0, United States of America

Huang, H.; Dabiri, D. & Gharib, M. (1997). On errors of digital particle image velocimetry, *Measurement Science Technology,* Vol. 8, No. 12, (December 1997), pp. 1427-1440, ISSN 0957-0233.

Keane, R. D. & Adrian, R. J. (1992). Theory of cross-correlation analysis of PIV images, *Applied Scientific Research*, Vol. 49, No. 3, (July 1992), pp. 191-215, ISSN 0003-6994.

Mackley, M. R. & Moore, I. P. T. (1986). Experimental velocity distribution measurements of high density polyethylene flowing into and within a slit, *Journal of Non-Newtonian Fluid Mechanics*, Vol. 21, No. 3, pp. 337-358, ISSN 0377-0257.

Migler, K. B.; Lavallée, C.; Dillon, M. P.; Woods, S. S. & Gettinger, C. L. (2001). Visualizing the elimination of sharkskin through fluoropolymer additives: Coating and polymer–polymer slippage, *Journal of Rheology,* Vol. 45, No. 2, (March 2001), pp. 565-581, ISSN 0148-6055.

Mitsoulis, E.; Kazatchkov, I. B. & Hatzikiriakos, S. G. (2005). The effect of slip in the flow of a branched PP melt: experiments and simulations, *Rheologica Acta*, Vol. 44, No. 4, (April 2005), pp. 418-426, ISSN 0035-4511.

Mooney, M. (1931). Explicit formulas for slip and fluidity, *Journal of Rheology,* Vol. 2, No. 2, (April 1931), pp. 210-222, ISSN 0148-6055.

Münstedt, H.; Schmidt, M. & Wassner, E. (2000). Stick and slip phenomena during extrusion of polyethylene melts as investigated by laser-Doppler velocimetry, *Journal of Rheology,* Vol. 44, No. 2, (March 2000), pp. 413-427, ISSN 0148-6055.

Nigen, S.; El Kissi, N.; Piau, J. M. & Sadun, S. (2003). Velocity field for polymer melts extrusion using particle image velocimetry: Stable and unstable flow regimes, *Journal of Non-Newtonian Fluid Mechanics*, Vol. 112, No. 2-3, (June 2003), pp. 177-202, ISSN 0377-0257.

Petrie, C. J. S. & Denn, M. M. (1976). Instabilities in polymer processing, *A.I.Ch.E. Journal,* Vol. 22, No. 2, (March 1976), pp. 209-236, ISSN 1547-5905.

Pérez-González, J. & de Vargas, L. (2002). Quantification of the slip phenomenon and the effect of shear thinning in the capillary flow of linear polyethylenes, *Polymer Engineering and Science,* Vol. 42, No. 6, (June 2002), pp. 1231-1237, ISSN 1548-2634.

Piau, J. M.; Kissi, N. & Mezghani, A. (1995). Slip flow of polybutadiene through fluorinated dies, *Journal of Non-Newtonian Fluid Mechanics*, Vol. 59, No. 1, (August 1995), pp. 11-30, ISSN 0377-0257.

Raffel, M.; Willer, C. E.; Wereley, S. T. & Kompehhans, J. (2007*). Particle Image Velocimetry. A Practical Guide*. (2nd edition), Springer-Verlag Berlin Hidelberg, ISBN 978-3-540-72307-3, Germany.

Robert, L.; Demay, L. & Vergnes, B. (2004). Stick-slip flow of high density polyethylene in a transparent slit die investigated by laser Doppler velocimetry, *Rheologica Acta*, Vol. 43, No. 1, (February 2004), pp. 89-98, ISSN 0035-4511.

Rodríguez-González, F.; Pérez-González, J.; de Vargas, L. & Marín-Santibáñez, B. M. (2010). Rheo-PIV analysis of the slip flow of a metallocene linear low-density polyethylene melt, *Rheologica Acta*, Vol. 49, No. 2, (February 2010), pp. 145-154, ISSN 0035-4511.

Rodríguez-González, F.; Pérez-González, J.; Marín-Santibáñez, B. M. & de Vargas, L. (2009). Kinematics of the stick–slip capillary flow of high-density polyethylene, *Chemical Engineering Science*, Vol. 64, No. 22, (November 2009), pp. 4675-4683, ISSN 0003-2509.

Scarano, F. & Riethmuller, M. L. (1999). Iterative multigrid approach in PIV image processing wiyh discrete window offset, *Experiments in Fluids*, Vol. 26, No. 6, (May 1999), pp. 513-523, ISSN 0723-4864.

Schmidt, M.; Wassner, E. & Münstedt, H. (1999). Setup and Test of a Laser Doppler Velocimeter for Investigations of Flow Behaviour of Polymer Melts. *Mechanics of*

Time-Dependent Materials, Vol. 3, No. 4, (December 1999), pp. 371-393, ISSN 1385-2000.

Shaw, M. T. (2007). Detection of multiple flow regimes in capillary flow at low shear stress, *Journal of Rheology,* Vol. 51, No. 6, (November 2007), pp. 1303-1318, ISSN 0148-6055.

Wassner, E.; Schmidt, M. & Münstedt, H. (1999). Entry flow of a PE-LD melt into a slit die: An experimental study by laser-Doppler velocimetry, *Journal of Rheology*, Vol. 43, No. 6, (November 1999), pp. 1339-1353, ISSN: 0148-6055.

Wereley, S. T. & Meinhart, C. D. (2001). Second-order accurate particle image velocimetry, *Experiments in Fluids*, Vol. 31, No. 3, (September 2001), pp. 258-268, ISSN 0723-4864.

Westerweel, J. (1994). Efficient detection of spurious vectors in particle image velocimetry data, *Experiments in Fluids*, Vol. 16, No. 3-4, (February 1994), pp. 236-247, ISSN 0723-4864.

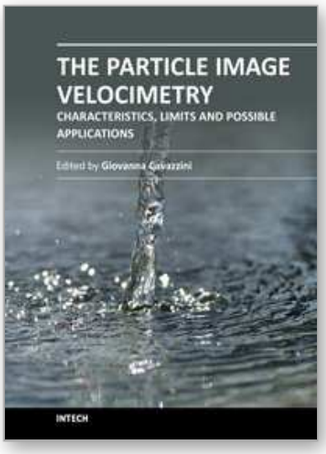

The Particle Image Velocimetry - Characteristics, Limits and Possible Applications

Edited by PhD. Giovanna Cavazzini

ISBN 978-953-51-0625-8
Hard cover, 386 pages
Publisher InTech
Published online 23, May, 2012
Published in print edition May, 2012

The Particle Image Velocimetry is undoubtedly one of the most important technique in Fluid-dynamics since it allows to obtain a direct and instantaneous visualization of the flow field in a non-intrusive way. This innovative technique spreads in a wide number of research fields, from aerodynamics to medicine, from biology to turbulence researches, from aerodynamics to combustion processes. The book is aimed at presenting the PIV technique and its wide range of possible applications so as to provide a reference for researchers who intended to exploit this innovative technique in their research fields. Several aspects and possible problems in the analysis of large- and micro-scale turbulent phenomena, two-phase flows and polymer melts, combustion processes and turbo-machinery flow fields, internal waves and river/ocean flows were considered.

How to reference

In order to correctly reference this scholarly work, feel free to copy and paste the following:

Jose Perez-Gonzalez, Benjamin M. Marin-Santibanez, Francisco Rodriguez- Gonzalez and Jose G. Gonzalez-Santos (2012). Rheo-Particle Image Velocimetry for the Analysis of the Flow of Polymer Melts, The Particle Image Velocimetry - Characteristics, Limits and Possible Applications, PhD. Giovanna Cavazzini (Ed.), ISBN: 978-953-51-0625-8, InTech, Available from: http://www.intechopen.com/books/the-particle-image-velocimetry-characteristics-limits-and-possible-applications/rheo-particle-image-velocimetry-for-the-analysis-of-the-flow-of-polymer-melts

INTECH
open science | open minds

InTech Europe
University Campus STeP Ri
Slavka Krautzeka 83/A
51000 Rijeka, Croatia
Phone: +385 (51) 770 447
Fax: +385 (51) 686 166
www.intechopen.com

InTech China
Unit 405, Office Block, Hotel Equatorial Shanghai
No.65, Yan An Road (West), Shanghai, 200040, China
中国上海市延安西路65号上海国际贵都大饭店办公楼405单元
Phone: +86-21-62489820
Fax: +86-21-62489821